

IMAGES OF THE RADIATIVELY INEFFICIENT ACCRETION FLOW SURROUNDING A KERR BLACK HOLE: APPLICATION IN SGR A*

YE-FEI YUAN¹, XINWU CAO², LEI HUANG^{1,2,3} AND ZHI-QIANG SHEN²

Submitted to ApJ

ABSTRACT

In fully general relativity, we calculate the images of the radiatively inefficient accretion flow (RIAF) surrounding a Kerr black hole with arbitrary spins, inclination angles, and observational wavelengths. For the same initial conditions, such as the fixed accretion rate, it is found that the intrinsic size and radiation intensity of the images become larger, but the images become more compact in the inner region, while the size of the black hole shadow decreases with the increase of the black hole spin. With the increase of the inclination angles, the shapes of the black hole shadows change and become smaller, even disappear at all due to the obscuration by the thick disks. For median inclination angles, the radial velocity observed at infinity is larger because of both the rotation and radial motion of the fluid in the disk, which results in the luminous part of the images is much brighter. For larger inclination angles, such as the disk is edge on, the emission becomes dimmer at longer observational wavelengths (such as at 7.0mm and 3.5mm wavelengths), or brighter at shorter observational wavelengths (such as at 1.3 mm wavelength) than that of the face on case, except for the high spin and high inclination images. These complex behaviors are due to the combination of the Lorentz boosting effect and the radiative absorption in the disk. We hope our results are helpful to determine the spin parameter of the black hole in low luminosity sources, such as the Galactic center. A primary analysis by comparison with the observed sizes of Sgr A* at millimeters strongly suggests that the disk around the central black hole at Sgr A* is highly inclined or the central black hole is rotating fast.

Subject headings: black hole physics – Galaxy: center – radiation transfer – sub-millimeter

1. INTRODUCTION

More and more observations indicate that supermassive black holes reside in most local galaxies, and the evolution of galaxies, quasars and supermassive black holes was realized in last decade (e.g., Ferrarese & Merritt 2000; Gebhardt et al. 2000; Hopkins et al. 2008). From the stellar dynamics, it is not surprising to find that the compact radio source Sagittarius (Sgr) A* at the center of our Galaxy is associated with a $\sim 4 \times 10^6 M_{\odot}$ massive dark object (Schödel et al. 2003; Ghez et al. 2005; Ghez et al. 2008). A natural candidate of the massive dark object is massive black hole, as emphasized by Kormendy & Richstone (1995), they argued convincingly that this object is a black hole, and the other alternatives to a black hole should be ruled out. Some of these alternatives have already been excluded. They include a cluster of dark objects, such as the stellar remnants or brown dwarfs (Maoz 1998), a binary made of point masses, self gravitationally supported Fermi ball (Miller 2006; Tsiklauri & Viollier 1998; Munyaneza et al. 1998; Yuan, Narayan, & Rees 2004). Another alternative which is still waiting for being excluded is self gravitationally supported boson ball (Torres et al. 2000; Yuan, Narayan, & Rees 2004). However, the problem of this model is that the mass of bosons is arbitrarily assumed to make a massive boson ball, and the energy dissipation between bosons may lead to the collapse of the ball (Maoz 1998).

Recent very-long baseline interferometry (*VLBI*) observation at the wavelength of 3.5mm shows its intrinsic size is 0.126 ± 0.017 mas, about $\sim 1AU$, and the resulting lower limit of its mass density is $6.5 \times 10^{21} M_{\odot} pc^{-3}$ (Shen et al. 2005), and the *VLBI* observation at 1.3mm gives the intrinsic size $0.037^{+0.016}_{-0.010}$ mas, and the resulting lower limit of its mass density is $9.3 \times 10^{22} M_{\odot} pc^{-3}$ (Doeleman et al. 2008), which strongly supports that Sgr A* is a supermassive black hole. The millimeter *VLBI* observation has been used to estimate the parameters of SgrA* accretion flow (Broderick et al. 2008). In the near future, higher resolution observations of Sgr A* at infrared (Paumard et al. 2005) and sub-millimeter wavelengths will be available (Doeleman & Bower 2004; Miyoshi et al. 2004; Fish et al. 2008), which can provide a direct test of the physical processes under the strong gravity, such as the dynamics of the accreted gas, complex trajectories of photons, and so on. Therefore, it is necessary to investigate the images of the flux and polarization of realistic accretion flows (Yuan et al. 2004; Broderick & Loeb 2006a; Huang et al. 2007, 2008), and the images and light curves associated with a hot spot in the accretion flow near the black hole horizon (Broderick & Loeb 2005, 2006b), the hot spot is proposed to explain the observations of near-infrared and X-ray flaring of Sgr A*.

It is generally believed that Sgr A* was a low luminosity AGN whose activity was switched off due to insufficient

¹ Key Laboratory for Research in Galaxies and Cosmology, University of Sciences and Technology of China, Chinese Academy of Sciences, Hefei 230026, China; yfyuan,mlhuang@ustc.edu.cn

² Key Laboratory for Research in Galaxies and Cosmology, Shanghai Astronomical Observatory, Chinese Academy of Sciences, Shanghai 200030, China; cxw,zshen@shao.ac.cn

³ Academia Sinica, Institute of Astronomy and Astrophysics, Taipei 106, Taiwan

gas supply (Narayan 2002). Multi-wavelength observations put strict constraints on theoretical accretion models of the massive black hole at the Galactic center. Among the theoretical models, the advection-dominated accretion flow (ADAF) model, also called the radiatively inefficient accretion flow (RIAF) model is claimed to be very successful in modeling the multi-wavelength spectrum from radio to X-ray (Narayan et al. 1995, 1998; Yuan et al. 2003, 2004). Based on the RIAF model, the images of Sgr A* at millimeter have been calculated, the size of the images is compared with observations to put an independent constraint on the RIAF model (Yuan et al. 2006; Huang et al. 2007), and the shape of the images, especially the location of the image centroid of Sgr A* can be used to determine the black hole spin (Broderick & Loeb 2006a).

There are several shortcomings in the previous calculations: first, although the treatment of the photon trajectories is within the framework of fully general relativity by using a ray tracing method, the accretion model is Newtonian, which means the global structure of the accretion flow is based on the Newtonian dynamics. The general relativity effect for the accretion flow is mimicked with Paczynski & Wiita potential. Therefore, the radial velocity of the accretion flow very close to the black hole is larger than the speed of light and thus is unphysical. Second, the massive black hole is assumed to be a non-rotating (Schwarzschild) hole in Yuan et al. (2004).

In this paper, following Manmoto (2000), the global structure of the relativistic ADAF around a Kerr black hole is derived to calculate the images of Sgr A* surrounding a Kerr black hole with an arbitrary black hole spin and viewing angle at several millimeter wavebands. Our treatment is within the framework of fully general relativity. A brief introduction to relativistic ADAF model is given in §2. The ray tracing method and the radiation transfer in curved space-time are discussed in §3. In §4, we summarize the key steps for calculating the images of ADAF of Sgr A*. The results and discussions are presented in §5 and §6, respectively.

2. GENERAL RELATIVISTIC RIAF MODEL

In the Boyer-Lindquist coordinates (t, r, θ, ϕ) , the Kerr metric is

$$ds^2 = -e^{2\nu} dt^2 + e^{2\psi} (d\phi - \omega dt)^2 + e^{2\mu_1} dr^2 + e^{2\mu_2} d\theta^2, \quad (1)$$

where

$$e^{2\nu} = \frac{\Sigma \Delta}{A}, \quad e^{2\psi} = \frac{A \sin^2 \theta}{\Sigma}, \quad e^{2\mu_1} = \frac{\Sigma}{\Delta}, \quad e^{2\mu_2} = \Sigma, \quad \omega = \frac{2ar}{A}, \quad (2)$$

$$\Delta = r^2 - 2r + a^2, \quad \Sigma = r^2 + a^2 \cos^2 \theta, \quad A = (r^2 + a^2)^2 - a^2 \Delta \sin^2 \theta. \quad (3)$$

Here, the notation in the seminal paper (Bardeen et al. 1972) has been taken, and the geometrical units $G = c = 1$ are used throughout this paper. The accretion flow has both azimuthal and radial motion in the accretion flow. The velocity field of the fluid is described by Ω and V , where Ω is the azimuthal angular velocity of the fluid and V is the physical velocity of the fluid with respect to the co-rotating reference frame which is carried by the observers with the four velocity $u^\mu = u^t(1, 0, 0, \Omega)$ (Abramowicz et al. 1997; Peitz & Appl 1997; Gammie & Popham 1998; Manmoto 2000). The four velocity of the fluid is (see the Appendix for the details)

$$u^\mu = (\gamma_r \gamma_\phi e^{-\nu}, \gamma_r \beta_r e^{-\mu_1}, 0, u^t \Omega). \quad (4)$$

In order to solve the global solution of the RIAF in Kerr metric, we follow Manmoto (2000) to formulate the fully relativistic hydrodynamical equations for RIAF. For simplicity, they assume the height of the accretion flow $H \leq r$, therefore the Boyer-Lindquist coordinates (t, r, θ, ϕ) are expanded around the equatorial plane up to $(z/r)^0$ terms to obtain a cylindrical coordinates (t, \tilde{r}, ϕ, z) . Another approximation is generally taken in previous investigations: the vertical integration. Therefore, all the physical quantities are taken their values at the equatorial plane. We employ the approach suggested by Manmoto (2000) to calculate the global structure of an accretion flow surrounding a massive black hole in the general relativistic frame, which allows us to calculate the structure of an accretion flow surrounding either a spinning or a non-spinning black hole. All the radiation processes are included in the calculations of the global accretion flow structure (see Manmoto 2000, for the details and the references therein). Integrating these equations from the outer boundary of the flow at $r = r_{\text{out}}$ inwards the black hole, we can obtain the global structure of the accretion flow passing the sonic point smoothly to the black hole horizon. Here, we allow the accretion rate of the accretion flow to vary with radius due to the putative winds (see Blandford & Begelman 1999, for the details), i.e., we assume the accretion rate $\dot{M}(r) = \dot{M}_0 (r/r_{\text{out}})^s$, where \dot{M}_0 is the accretion rate at the outer radius of the ADAF (Yuan et al. 2003).

The global solution of general relativistic RIAF (GR-RIAF hereafter) has been obtained in the previous works, and the effects of black hole rotation have been discussed in the great details (Gammie & Popham 1998; Popham & Gammie 1998; Manmoto 2000). In order to help understand our numerical results, the global solution of ADAF is shown in Fig.1. The basic parameters are taken as follows: the black hole mass of Sgr A* $M_{\text{bh}} = 4 \times 10^6 M_\odot$, the wind index $s = 0.25$, the fraction of the dissipated power directly heating the electrons $\delta = 0.3$, the accretion rate at the outer radius $\dot{M}_0 = 0.7 \times 10^{-6} M_\odot \text{yr}^{-1}$, the ratio of the gas pressure to the total pressure $\beta = 0.95$. These parameters are the same as the RIAF parameters in Yuan et al. (2006)'s work, except the slightly difference in accretion rate (see §5 for the discussion). It should be emphasized that the ion and electron temperatures increase significantly within $10^2 R_g$ with the increase of the black hole spin parameter from $a = 0$ to $a = 0.998$, and decrease, with less difference, with its decrease from $a = 0$ to $a = -0.998$. Similar changes appear in electron number density and magnetic field

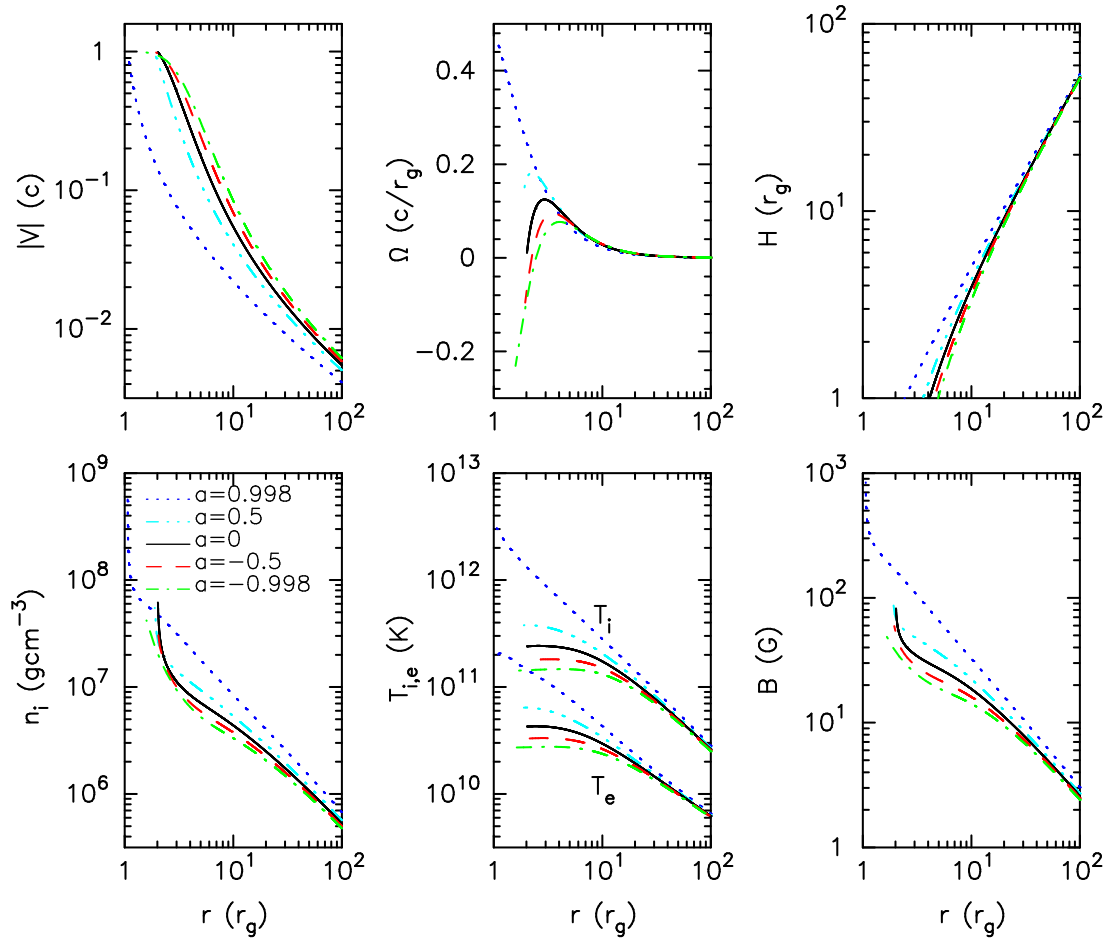


FIG. 1.— Global solution of GR-ADAF. The solid lines represent the results for $a = 0$, the dotted lines the results for $a = 0.998$, the dotted-dashed lines the results for $a = 0.5$, the dashed lines the results for $a = -0.5$, and the dotted-dashed lines the results for $a = -0.998$. Except the upper left panel, the lines above the solid ones represent the results for prograde disks ($a > 0$), while the lines below the results for retrograde disks ($a < 0$). *Upper left*: Radial velocity V as a function of radii. The lines below the solid ones are for $a > 0$, while the lines above are for $a < 0$. *Upper middle*: Coordinate angular velocity Ω . *Upper right*: The half height of the disk H . *Lower left*: The number density of ions versus radii. *Lower middle*: The temperature of ions and electrons. *Lower right*: The magnetic field B which is deduced from the global solution of ADAF.

strength. Because the radio emission is mainly from the synchrotron radiation which depends sensitively on electron temperature, the effects of the black hole spin on the radio emission is mainly through its effects on the electron temperature.

3. RELATIVISTIC RADIATION TRANSFER OF PHOTONS FROM GR-RIAF

In this paper, the images of Sgr A* modeled as a GR-RIAF surrounding a massive black hole are calculated. In our calculations, we do not consider the Compton effect of photons at radio wavelength, because the relativistic electrons will boost the low energy photons to higher energy which is beyond our interest. As a bunch of photons travel along their geodesics, some of them will be absorbed due to synchrotron self-absorption in the accretion flow, while some of new photons will be added due to the emission of the flow. To solve the radiation transfer of radio photons, we should first determine their trajectories using the ray tracing method.

3.1. Ray Tracing Method

In the Kerr space-time, all of the four constants for the motion of a test particle have been found by Carter (1968), they are the energy at infinity

$$E = -p_t, \quad (5)$$

the effective angular momentum,

$$L_z = p_\phi, \quad (6)$$

the Carter constant,

$$Q = p_\theta^2 - a^2 E^2 \cos^2 \theta + L_z^2 \cot^2 \theta, \quad (7)$$

and the Hamiltonian constant,

$$H = \frac{1}{2} \epsilon = \frac{1}{2} p^\mu p_\mu, \quad (8)$$

where $\epsilon = 0$ for massless particles such as photons, or $\epsilon = 1$ for massive particles. Therefore, given three constants of motion, i.e. E, L_z, Q , the trajectory of a photon can be determined. As the trajectory of a photon is independent on its energy, it can be completely determined by the two dimensionless parameters $\lambda = L_z/E$ and $q = Q^{1/2}/E$. Furthermore, Cunningham & Bardeen (1973) pointed out that the two parameters λ and Q are related to the two impact parameters α and β that describe the apparent position of the image on the sky as seen by an observer at infinity who receives that light ray,

$$\alpha = - \left(\frac{rp^{(\phi)}}{p^{(t)}} \right)_{r \rightarrow \infty} = - \frac{\lambda}{\sin \theta_{\text{obs}}}, \quad (9)$$

$$\beta = \left(\frac{rp^{(\theta)}}{p^{(t)}} \right)_{r \rightarrow \infty} = (q + a^2 \cos^2 \theta_{\text{obs}} - \lambda^2 \cot^2 \theta_{\text{obs}})^{1/2} = p_{\text{obs}}, \quad (10)$$

where θ_{obs} is the angular coordinate of the observer at infinity and $p^{(a)}$ is the four momentum in the locally non-rotating frame (see the Appendix). The direction of β points along the projected direction of the spin axis of black hole. Due to the azimuthal symmetry, the photon trajectory originating from a position (r, θ) to the observer at infinity whose angular coordinate is θ_{obs} can be solved by the following integral equation:

$$\pm \int_r^\infty \frac{dr}{\sqrt{R(r; \lambda, q)}} = \pm \int_\theta^{\theta_{\text{obs}}} \frac{d\theta}{\sqrt{\Theta(\theta; \lambda, q)}} = P, \quad (11)$$

where

$$R(r; \lambda, q) = r^4 + (a^2 - \lambda^2 - q)r^2 + 2[q + (\lambda - a)^2]r - a^2q, \quad (12)$$

$$\Theta(\theta; \lambda, q) = (q + a^2 \cos^2 \theta - \lambda^2 \cot^2 \theta). \quad (13)$$

The signs in the above integrals must be the same as those of dr and $d\theta$ to guarantee the integral P is always positive and increasing along a photon's trajectory. Therefore, the signs change at the turning points in r and θ , where $R(r; \lambda, q) = 0$ or $\Theta(\theta; \lambda, q) = 0$ respectively. It is important to realize that both $R(r)$ and $\Theta(\theta)$ are quartic polynomials of r and θ respectively, therefore both integrals in Eq. (11) can be integrated in terms of elliptic functions (Chandrasekhar 1983; Rauch & Blandford 1994; Cadez et al. 1998).

Owing to above observations, a photon trajectory can be determined by using a ray tracing method: first, given α and β which determine the position of the image in the photo-graphical plate of an observer with θ_{obs} , the two constants of motion are obtained, according to Eqs. (9-10). Second, given the integral P , which can be understood as the affine parameter along the photon's trajectory, the position of the photon can be determined using the expression of Eq.(11) as elliptic functions:

$$r = r(P; \lambda, q), \quad (14)$$

$$\theta = \theta(P; \lambda, q). \quad (15)$$

3.2. Relativistic Radiation Transfer

Given the two constants of motion of a photon, its momentum has components,

$$k_\mu = g_{\mu\nu} \frac{dx^\nu}{d\sigma} = (k_t, k_r, k_\theta, k_\phi) = \left(-1, \pm \frac{\sqrt{R}}{\Delta}, \pm \sqrt{\Theta}, \lambda \right) \quad (16)$$

where σ is the affine parameter of photon's trajectory, and E is absorbed into σ . The signs in the above equation are the same as those of dr and $d\theta$. Suppose the photon frequency observed by the observer at infinity is ν_{obs} , then the emitting frequency at the locally rest frame of the fluid (LRF) is

$$\nu_{\text{em}} = -(k_\mu u^\mu) \nu_{\text{obs}}, \quad (17)$$

where u^μ is the four velocity of the fluid. In the LRF, the radiation transfer equation is (Rybicki & Lightman 1979)

$$\frac{dI(\nu_{\text{em}})}{dL} = -\kappa(\nu_{\text{em}})I(\nu_{\text{em}}) + \eta(\nu_{\text{em}}), \quad (18)$$

where I is the radiation intensity of photons and dL is the element of physical distance of photon traveling in LRF. As $\mathcal{I} \equiv I/\nu^3$ is a Lorentz invariant, the above equation can be re-written as follows,

$$\frac{d\mathcal{I}(\nu_{\text{em}})}{dL} = -\kappa(\nu_{\text{em}})\mathcal{I}(\nu_{\text{em}}) + \frac{\eta(\nu_{\text{em}})}{\nu_{\text{em}}^3}. \quad (19)$$

Since the speed of light is $c = 1$, we have

$$\frac{dL}{d\sigma} = \frac{dx^{(0)}}{d\sigma} = \frac{dx^\mu}{d\sigma} e_\mu^{(0)}(\text{LRF}) = -k_\mu u^\mu. \quad (20)$$

Therefore, the radiation transfer equation in curved space-time reads (Fuerst & Wu 2004),

$$\frac{d\mathcal{I}(\nu_{\text{em}})}{d\sigma} = -k_{\mu}u^{\mu}[-\kappa(\nu_{\text{em}})\mathcal{I}(\nu_{\text{em}}) + \eta(\nu_{\text{em}})/\nu_{\text{em}}^3] \quad (21)$$

$$= [-\nu_{\text{em}}\kappa(\nu_{\text{em}})\mathcal{I}(\nu_{\text{em}}) + \eta(\nu_{\text{em}})/\nu_{\text{em}}^2]/\nu_{\text{obs}}. \quad (22)$$

It is well known that \mathcal{I} , $\nu\kappa(\nu)$, and $\eta(\nu)/\nu^2$ are Lorentz invariants (Rybicki & Lightman 1979), therefore, the above radiation transfer equation is written in the Lorentz invariant form as we expected.

Since

$$\Sigma \frac{dr}{d\sigma} = \pm\sqrt{R}, \quad (23)$$

$$\frac{dr}{dP} = \pm\sqrt{R}, \quad (24)$$

therefore,

$$d\sigma = -\Sigma dP. \quad (25)$$

Introducing $\tilde{\kappa} = \nu_{\text{em}}\kappa(\nu_{\text{em}})/\nu_{\text{obs}}$ and $\tilde{\eta} = \eta(\nu_{\text{em}})/(\nu_{\text{em}}^2\nu_{\text{obs}})$, and the formal solution to the transfer equation reads,

$$\mathcal{I}(\infty) = \int_0^{P_{\text{max}}} \exp\left(-\int_{P'}^{P_{\text{max}}} \tilde{\kappa}(P'')\Sigma dP''\right) \tilde{\eta}(P')\Sigma dP', \quad (26)$$

where P_{max} is the maximal trajectory integral tracing from the infinity to the innermost emitting position.

4. IMAGES OF GR-RIAF AT MILLIMETER WAVELENGTHS

After solving the global structure of the RIAF around a Schwarzschild or Kerr black hole, the physical quantities at the equatorial plane have been obtained, such as:

$$n_e(\tilde{r}, z=0), n_i(\tilde{r}, z=0), V_r(\tilde{r}, z=0), \Omega(\tilde{r}, z=0). \quad (27)$$

In the following calculations, the isothermal approximation is taken in the vertical direction, therefore, the density distribution in the vertical direction is:

$$n_e(\tilde{r}, z) = n_e(\tilde{r}, z=0) \exp(-z^2/2H^2),$$

$$n_i(\tilde{r}, z) = n_i(\tilde{r}, z=0) \exp(-z^2/2H^2),$$

and

$$V_r(\tilde{r}, z) = V_r(\tilde{r}, z=0),$$

$$\Omega(\tilde{r}, z) = \Omega(\tilde{r}, z=0).$$

At any position along the photon trajectory, such as $(r(P), \theta(P))$, we can determine $u^{\mu}(P)$ and $k_{\mu}(P)$, so we get $\nu_{\text{em}}(P) = (-u^{\mu}(P)k_{\mu}(P))\nu_{\text{obs}}$. The magnitude of magnetic field $B(\tilde{r}, z)$ is determined by the local physical conditions:

$$P_{\text{gas}}(\tilde{r}, z) = n_i(\tilde{r}, z)k_{\text{B}}T_i + n_e(\tilde{r}, z)k_{\text{B}}T_e,$$

$$P_{\text{mag}}(\tilde{r}, z) = P_{\text{gas}}(\tilde{r}, z)(1 - \beta)/\beta,$$

$$B(\tilde{r}, z) = \sqrt{8\pi P_{\text{mag}}}$$

The emissivity and absorption coefficients at each position can be calculated, considering the bremsstrahlung and synchrotron radiation mechanism. The Compton scattering effect is ignored, because it generally produces photons at higher wavelength band which are not interested in this work. Finally, the radiation intensity received by the observer at infinity can be calculated according to Eq.(26).

5. NUMERICAL RESULTS

In the work of Yuan et al. (2006), the size of Sgr A* was calculated in the RIAF model of Yuan et al. (2003). In this RIAF model, the accretion rate is assumed to be $\dot{M}(r) = \dot{M}_0(r/r_{\text{out}})^s$ due to the presence of winds, where \dot{M}_0 is the accretion rate at the outer radius of the RIAF (Yuan et al. 2003). The black hole mass of Sgr A* $M_{\text{bh}} = 4 \times 10^6 M_{\odot}$ is adopted in their work, which is different from $M_{\text{bh}} = 2.5 \times 10^6 M_{\odot}$ adopted in Yuan et al. (2003). Thus, they tuned the parameters of the RIAF in order to reproduce the observed spectrum in different wavebands, which leads to $s = 0.25$, the fraction of the dissipated power directly heating the electrons $\delta = 0.3$. Their calculations of the RIAF structure were carried out by adopting the Pseudo-Newtonian potential. Compared with the results in fully general relativistic frame in the case of a Schwarzschild black hole (i.e., $a = 0$), their global solution of the RIAF deviates only slightly in region out of $\sim 20R_g$, but to a certain extent in the inner region within $\sim 20R_g$. In this work, we simply adopt the same RIAF parameters as in Yuan et al. (2006) in all our calculations independent of black hole spin parameter a ,

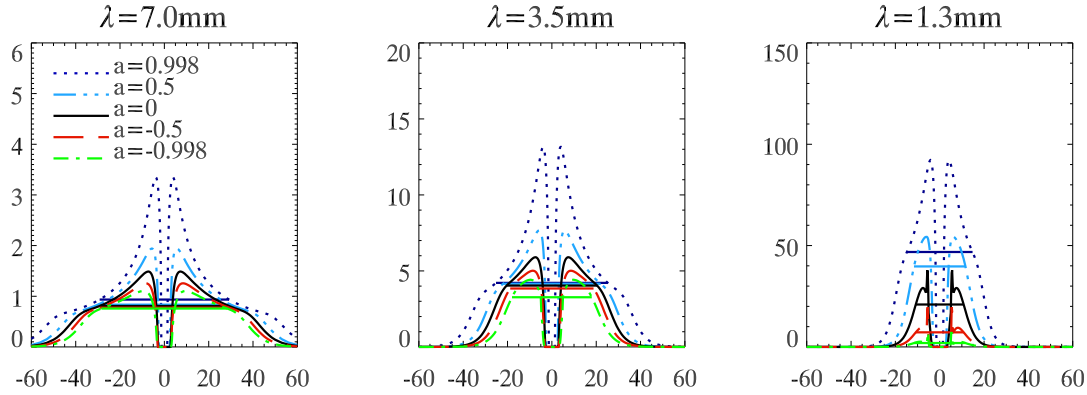


FIG. 2.— Intensity of the ADAF around Kerr black holes with different spins at the wavelengths of $\lambda = 7.0\text{mm}$, 3.5mm , 1.3mm (columns from left to right) as a function of α (or β) when $\theta_{\text{obs}} = 0^\circ$. Results for different spin parameter a are shown in line styles the same as those in Fig.1. The horizontal lines show the intrinsic size of the disk which is defined according to Eq.(28)-(29).

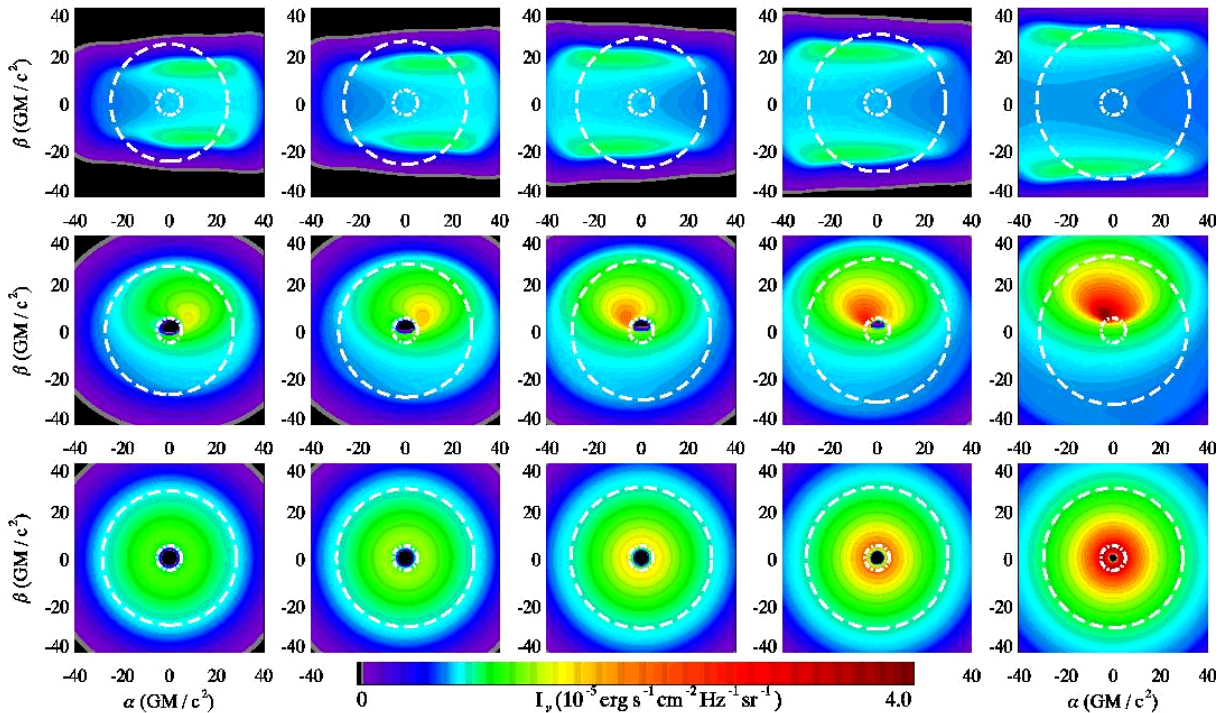


FIG. 3.— Images at wavelength of 7.0mm of the ADAF of Kerr black holes with spins $a = -0.998, -0.5, 0, 0.5, 0.998$ (from left to right) and with the viewing angles $\theta_{\text{obs}} = 90^\circ, 45^\circ, 0^\circ$ (from top to bottom). The spin of the black hole is along the perpendicular direction. The diameter of the dash-dotted circle is twice the photon capture impact parameter ($2\sqrt{27}M$). The diameter of the dashed circle is the intrinsic size (D_{ch}) of each image, see definition in the text. To show relative radiation intensity, the range of the intensity is scaled together for all the panels.

except that a slightly lower accretion rate ($\dot{M} = 0.7 \times 10^{-6} M_{\odot} \text{yr}^{-1}$, 70 percent of that adopted by Yuan et al. (2006)) at the outer boundary of the RIAF is adopted in our calculations, which can compensate the discrepancy between our GR-RIAF solution and the RIAF solution of Yuan et al. (2006) in the inner region of the flow near the black hole with $a = 0$. We find that our global GR-RIAF solution can reproduce the broad spectrum from radio to X-ray quite well for a non-rotating black hole while viewed face-on. We treat this as our fiducial model. In principle, we should have to tune the RIAF parameters to fit the observed spectrum, the size of the scattered images, and even the polarization properties, whenever the black hole spin parameter a and the inclination angle θ_{obs} are specified as done in Broderick et al. (2008), but this is very cumbersome and beyond the scope of this work, which should be carried out in our later work. To focus on the influence of black hole spin on the general properties of the images at millimeter wavelengths, as a first step, we will not change any RIAF parameters in our calculations for the GR-RIAF structure, except for different values of black hole spin parameters. Because the non-thermal electrons are artificially added to explain the observed long wavelength ($\gtrsim 7\text{mm}$) radio spectrum, we consider the radio emission is contributed only from the thermal electrons in the following calculations.

Following the procedures described in the previous sections, we calculate the images of GR-RIAF around a black hole with arbitrary spins, inclination and at different observational wavelengths. Our results are shown in Fig.2-5,

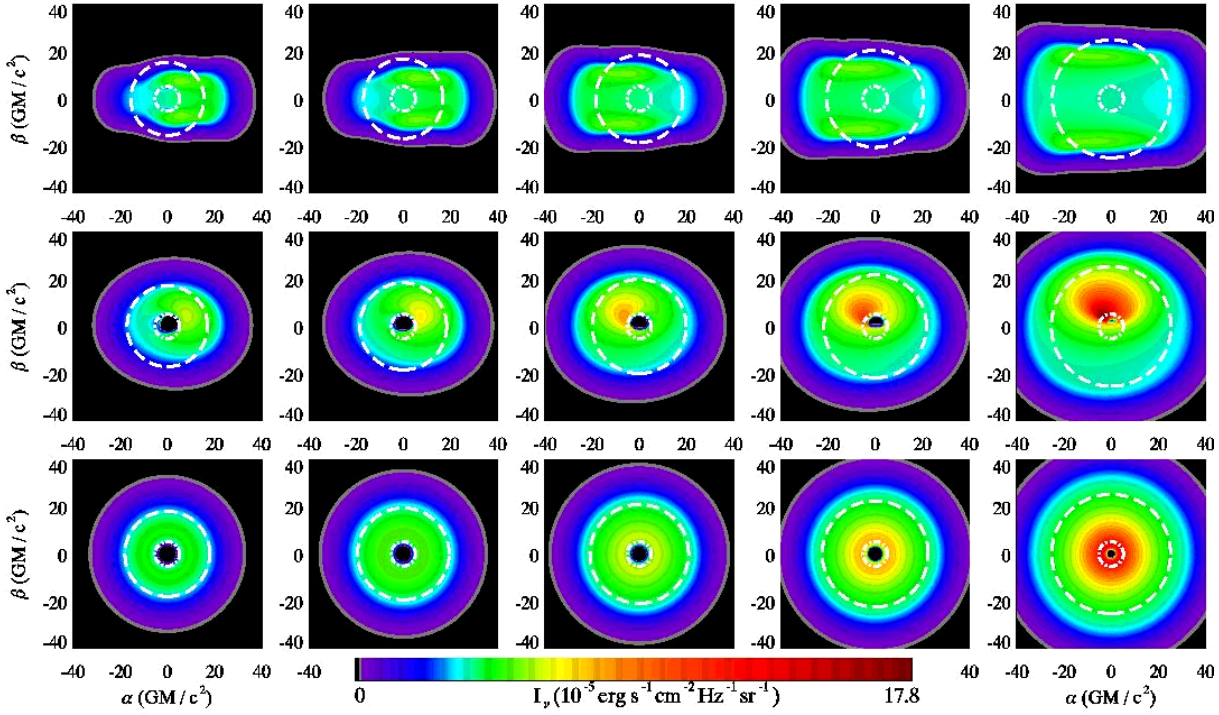


FIG. 4.— As in Fig.3, but images at the wavelength of 3.5mm.

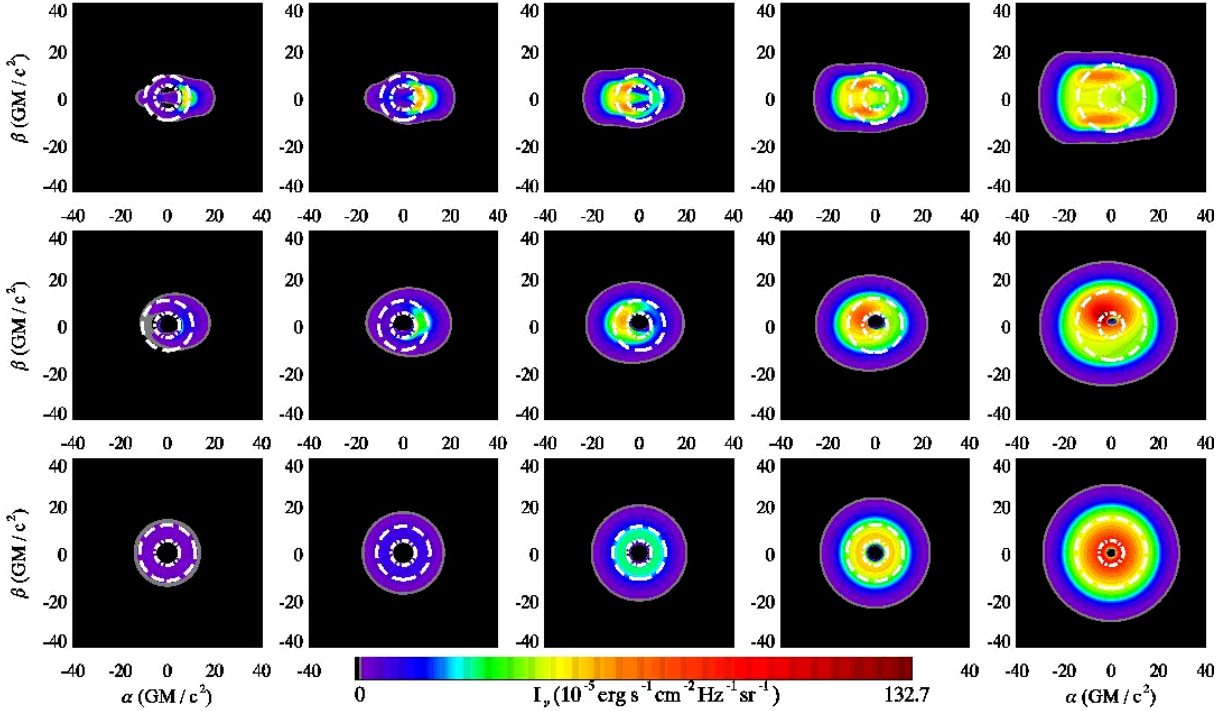


FIG. 5.— As in Fig.3, but images at the wavelength of 1.3mm.

respectively.

Figure 2 shows the results for face on case, i.e., the radiation intensity of GR-RIAF around a black hole as a function of α (or β , because of the symmetry of the system) for $a = 0, \pm 0.5, \pm 0.998$ and for millimeter wavelengths, $\lambda_{\text{obs}} = 7.0, 3.5, 1.3$ mm, in which we are most interested. Here we define the intrinsic size D_{ch} of the disk at a given

TABLE 1
SIZE (DIAMETER) OF THE SHADOW OF THE BLACK HOLE

Spin of the hole (a)	$\lambda = 7.0\text{mm}$ (M)	$\lambda = 3.5\text{mm}$ (M)	$\lambda = 1.3\text{mm}$ (M/ μas)
0.998	2.8	2.8	2.8/13.8
0.5	5.2	5.2	5.2/25.6
0	5.6	5.6	5.6/27.6
-0.5	6.0	6.0	6.4/31.5
-0.998	6.4	6.8	7.6/37.5

frequency as

$$\int_{\rho \lesssim D_{\text{ch}}/2} I_{\nu}(\alpha, \beta) d\Omega_{\text{obs}} = \varepsilon \int I_{\nu}(\alpha, \beta) d\Omega_{\text{obs}}, \quad (28)$$

where $\rho = \sqrt{\alpha^2 + \beta^2}$ is the distance to the mass center of the hole, Ω_{obs} is the observed solid angle, and the coefficient is the ratio of emission within the full width of half maximum (FWHM) of a 2-dimensional(2-d) Gaussian function $G(\alpha, \beta)$ to its total emission, i.e.,

$$\varepsilon = \frac{\int_{\rho \lesssim \text{FWHM}/2} G(\alpha, \beta) d\Omega_{\text{obs}}}{\int G(\alpha, \beta) d\Omega_{\text{obs}}}. \quad (29)$$

By convention of VLBI observation, FWHM is used to measure the size of a 2-d Gaussian distributed source.

For an image with the standard Gaussian distribution, the intrinsic size D_{ch} defined here reduces to its FWHM, therefore, for an image deviated from the Gaussian distribution, the intrinsic size can be considered as its equivalent FWHM. As seen from Fig.2, the radiation intensity I_{ν} increases with the increase of BH spin ranging from $a = -0.998$ to $a = 0.998$, while the intrinsic size of the disk, marked as region with radii covered by the horizontal lines for each case, increases in the same way. These results are expected from the effect of BH spin on the global solution of GR-RIAF (see Fig.1): the larger the BH spin, the higher the electron/ion number density and their temperature, and the larger magnetic field in the disk. Because the emissivity at radio wavebands is dominated by synchrotron radiation, larger spin leads to higher radiation intensity of the disk. As has been found in previous investigations, roughly the global solutions of GR-RIAF for $a > 0$ differ from that for $a = 0$ more than the corresponding $a < 0$ cases (Gammie & Popham 1998; Popham & Gammie 1998). This tendency is also reflected in Fig.2 for longer wavelength $\lambda_{\text{obs}} = 7.0, 3.5\text{mm}$. With the decrease of the wavelength, the emitting region becomes smaller, because the physical conditions in the inner region change dramatically, consequently, the difference among the final intensity in the inner region becomes larger, especially for $a > 0$ cases. The effect of the observational wavelength on the intrinsic size of the images is also clearly shown in Fig.2: the shorter the observational wavelength, the smaller the emitting region of the disk.

For a Schwarzschild black hole, the maximal impact factor for photon capture is $\sqrt{27}M$, therefore, the typical size of the BH shadow is the circle with diameter of $2\sqrt{27}M$. The size of the black hole shadow, region without any emission, are listed in Table 1. In the last column with $\lambda = 1.3\text{mm}$, the corresponding angular size is also listed.

In our calculation, the accretion flow extends to the horizon of the hole $r_{\text{h}+}$. It is well known that the larger the spin of the hole, the smaller its horizon and marginally stable orbit r_{ms} . This tendency is clearly shown in Table 1: it is found that the shadows of black hole decreases with the increase of spin of the hole, if the disk is prograde with the hole, whilst, if the disk is retrograde with the hole, the size of the shadow does not change significantly. For the same spin of the hole, the size of the shadow at different wavelength does not change significantly (see also Falcke et al. 2000; Broderick & Loeb 2006a,b; Takahashi 2004).

Figure 3-5 shows the images of the GR-RIAF around a black hole with different spin a , the inclination angle of the observer at infinity θ_{obs} , and at the different wavelength λ_{obs} . The observed images at 7.0mm for the prograde/retrograde disks with the black hole are shown in Fig.3. Each column corresponds to the results for different spin of the hole, from left to right, the spin of the hole is $a = -0.998, -0.5, 0, 0.5, 0.998$, respectively. Each rows corresponds to the different θ_{obs} , from top to bottom, $\theta_{\text{obs}} = 90^{\circ}, 45^{\circ}, 0^{\circ}$. For each image, its intrinsic size is plotted in a white dashed circle, emission within which is equal to ε which is defined in Eq. (29) times its total emission. The photon capture region for a Schwarzschild black hole is also plotted in a white dash-dotted circle for reference. All images in this figure are scaled in the same way to show clearly the relative radiation intensity for different spin and inclination.

In Figure 3, for the same inclination, the effects of spin on the size and intensity of the disk are similar: the larger the BH spin, the larger the emitting region, i.e., the intrinsic size, and the higher the radiation intensity. As increasing the inclination angle, the shadow of the images decreases due to the obscuration of the GR-RIAF with a finite height which is about $H \leq r$. For the extreme case of $\theta_{\text{obs}} = 90^{\circ}$, there is no shadow at all. When $\theta_{\text{obs}} = 45^{\circ}$, the luminous part of the images which is located at the left and top (for $a \geq 0$ cases), or right and top (for $a < 0$ cases) of the image is brighter than the luminous part of the images for $\theta_{\text{obs}} = 0^{\circ}$. This is due to the Lorentz boosting effects: at the left and top (or right and top) of the disk, the fluid has the larger radial velocity to the observer at infinity because of the rotation and radial motion of the accretion flow. For $\theta_{\text{obs}} = 90^{\circ}$, the radio emission is separated into two arcs for high spin (e.g. $a \geq 0.9$), while the weak radio emission appears between two arcs for low spin. Our analysis is as follows:

the photons from the central part travel through the most dense region near the equatorial plane of the disk, which results in the great absorption of the emission, therefore, the resulting emission is much weak. Radiative absorption is the reason why the luminous parts of the images are not at the central regions near the equatorial plane of the disk, and the intensity of the luminous parts is also lower than that of the corresponding face on cases. As discussed above, the intrinsic size decreases with the increasing of the inclination angle. However, such decrease becomes less significant for larger spin. For the $a = 0.998$ case, the intrinsic size nearly does not change. This can be explained as follows: for larger inclination angle, the obscuration of the disk decreases the emission, as well as the size of the emitting region. On the other hand, the light bends more significantly, bringing emission from the more inner region, therefore both the emission and emitting region increase. For an extremely-rotating ($a = 0.998$) black hole, the emitting region increased by its extremely curved space-time can almost compensate that decreased by inclination, although the emission is not compensated enough.

The images at 3.5mm and 1.3mm are shown in Fig. 4 and Fig. 5, respectively. The behavior of the images at 3.5mm and 1.3mm with varying the spin and the inclination are very similar to those at 7.0mm. The main differences are reflected in the intrinsic sizes of images. At shorter wavelength, the disk appears to be smaller than those at longer wavelength, this is because the shorter wavelength photons are from the more inner parts of the disk. For shorter wavelength photons emitting from the inner parts of the disk, their optical depth might be so significant, causing the shadow in the images of the disk even when $\theta_{\text{obs}} = 90^\circ$ for low spin. The size of the shadow is similar to the size of the circle with a radius of the photon capture impact parameter ($\sqrt{27}$)M. When the disk is edge on, for the longer wavelength of the observed photons, because the optical depth of the emitted photon near the equatorial plane is not so large that the shadow does not appear. For $\lambda_{\text{obs}} = 1.3\text{mm}$ and median spin $a \leq 0.5$, the luminous parts of the images are brighter than these of the corresponding face on cases, so that the larger inclination results in higher emission. This is because the Lorentz boosting effect dominates the radiative absorption. Exceptionally, at high spin, such as $a = 0.998$ and $\theta_{\text{obs}} = 90^\circ$, the emitting region is near to the horizon of the black hole, thus, the radiative absorption dominates the Lorentz boosting, as a result, the intensity of the luminous parts is lower than that of the corresponding face on cases as in Fig. 3 and Fig. 4 for longer wavelengths.

6. DISCUSSIONS

In this work, the images of the GR-RIAF around a Kerr black hole are simulated. The main results are summarized as follows: 1) the effects of BH spin: the larger the spin, the smaller the size of black hole shadow, which is similar to the previous results (e.g., Falcke et al. 2000; Broderick & Loeb 2006a,b; Takahashi 2004). The larger the spin, the larger the intrinsic size of the image, and the brighter the whole disk, especially its inner part. These effects are more significant in a prograde disk than a retrograde disk. We should emphasize that this contrasts with the result obtained in (Broderick & Loeb 2006a,b). The reason is that Broderick & Loeb (2006a,b) assumed a parameterized ADAF solution for a spinning black hole which is required to fit the observed spectrum, therefore, they found that the thermal electron density must decrease with increasing spin, as well with increasing inclination. More important is that the non-thermal electron density must increase, in order to produce the radio spectrum. However, in this work, we do all the calculation in the light of a fiducial GR-ADAF model in which the accretion rate is fixed. Consequently, the electron density increase with increasing spin (see Fig. 1). 2) the effects of the inclination: the larger the inclination angles, the smaller the size of black hole shadow, and the smaller the intrinsic size of the image. This is consistent with (Noble et al. 2007). If the disk is edge on, the shadow are even obscured at all. The central part of the image is both darkened by the absorption and brightened by the light bending, so that how the brightness of the image changes depends on the observational wavelength. 3) the effects of the observational wavelength: the shorter the observational wavelength, the smaller the intrinsic size of the image.

Although a larger spin makes the intrinsic size enlarged, it makes the total emission enhanced to a greater extent. This tendency differs from face-on to edge-on cases. At 7.0mm, for instance, as shown in Fig.3, an extremely-rotating black hole ($a = 0.998$) enhances $> 60\%$ total emission than a non-rotating black hole ($a = 0$) does. For the face-on case, however, the intrinsic size is enlarged only by $\approx 15\%$. For the same comparison at 3.5mm, as shown in Fig.4, the total emission is enhanced by $\approx 99\%$ while the intrinsic size is enlarged by only $\approx 23\%$. Therefore, more emission comes from the inner part of the image if the black hole spin increases.

As discussed in §5, in Yuan et al. (2006), the global structure of the RIAF were calculated by adopting Pseudo-Newtonian potential, and taking the non-thermal electrons into consideration. The disk is viewed as facing on, and the thickness of the disk is ignored. It was found that the scattered images are more extended than the observational images at both 7.0mm and 3.5mm (Shen et al. 2005). In our GR-RIAF model with the same parameters, the scattered images are even bigger. This is because the lower electron temperature and density are obtained in GR-RIAF model, enlarging the emission region. However, the overestimated intrinsic sizes do not imply an anti-rotating black hole, which predicts smaller intrinsic sizes. As mentioned above, this is because the anti-rotating black hole also predicts much lower total emission. The required emitting region should be enlarged a lot to produce the observed emission. On the other hand, a co-rotating black hole is preferred, since the required emitting region could be more compact.

For a primary application, we adjust the index of the wind index s and energy fraction of non-thermal electrons η to reproduce the spectrum of quiescent state of Sgr A*. Only face-on case is investigated as an example. For the Schwarzschild case, we choose $s = 0.285$ and $\eta = 0.4\%$, different from those in Yuan et al. (2006) due to the relativistic effects. In order to produce the observed the spectrum both in radio and sub-millimeter band, s should be decreased, while η should be increased for a faster co-rotating black hole. Contrarily, for a faster anti-rotating black hole, s should be increased while η should be decreased for the same purpose. In Fig.6, the predicted spectra, the FWHM

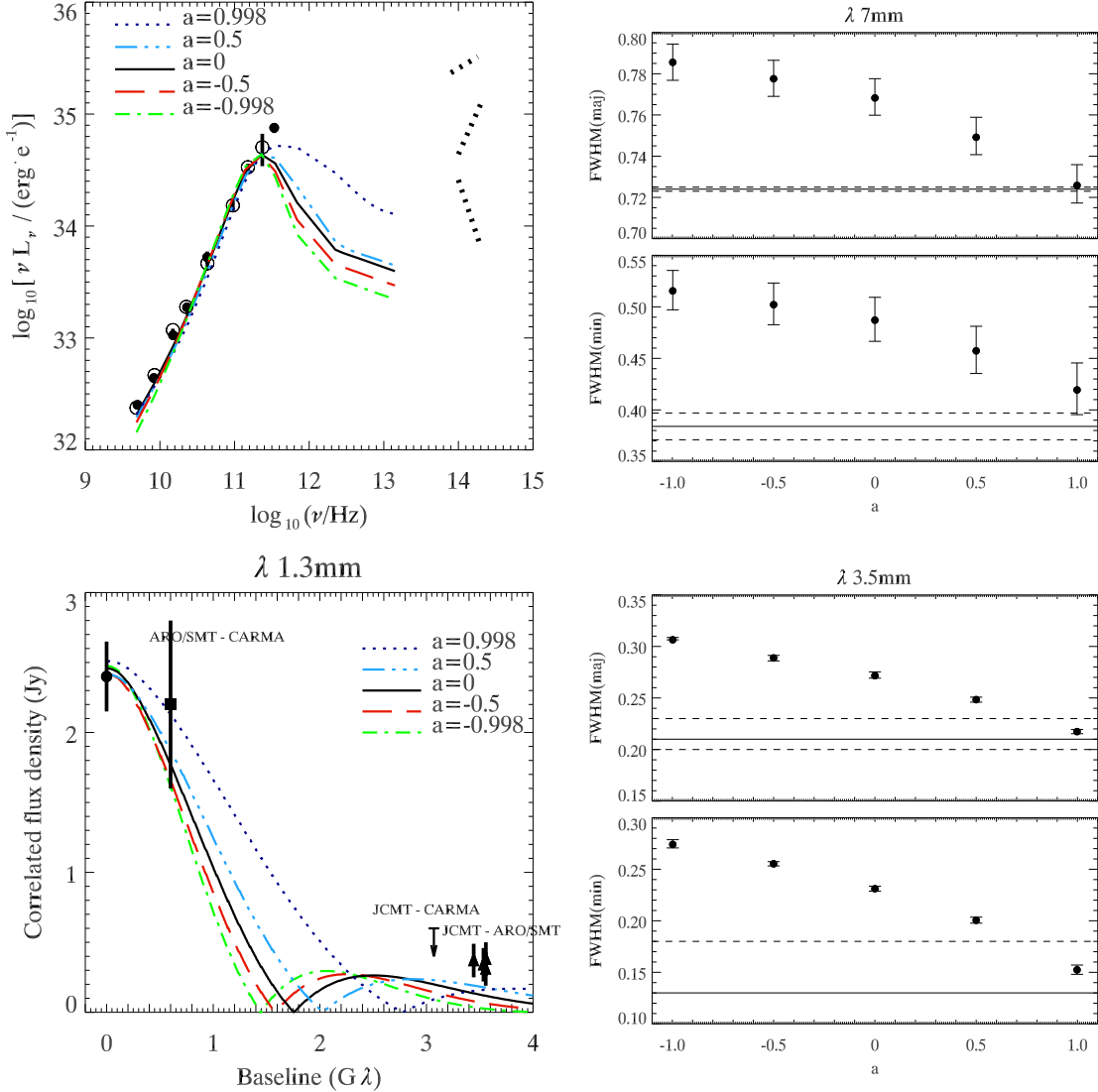


FIG. 6.— Spectra, full-width of half maximum of the scatter-broadened image at 7.0mm and 3.5mm, and visibility profiles at 1.3mm for Sgr A*, predicted by face-on GR-RIAF with $a = -0.998, 0.5, 0, 0.5$ and 0.998 . See the details in the text.

of the images at 7.0mm and 3.5mm, and the visibility profiles at 1.3mm are shown for five examples with different spins, with the interstellar scattering effect having been taken into consideration. As expected, the smaller sizes are obtained at all the three wavelengths for a higher spin. Compared with the measured sizes at 7.0mm and 3.5mm by Shen et al. (2005), the predicted FWHMs are plotted in the solid and dashed lines for averages and limits in the right two panels of Fig.6, respectively. It is strongly indicated in Fig.6 that a fast co-rotating black hole is preferred, if the disk is facing on. Notice that the FWHM of the minor axis at 7.0mm overestimates the observation, even with an extremely rotating black hole. This may imply an inclined disk which makes the intrinsic sizes smaller (see section 5). By analyzing the existing spectral and polarization measurements, Broderick et al. (2008) found that low values of the inclination angle are excluded, which is consistent with our analysis.

The VLBI observations also predict that the black hole shadow structure is hoped to be resolved if the observational wavelength decreases to 1.3mm. The scattering size extrapolated from previous longer wavelength observations is $\sim 23\mu\text{as}$, which means any structure with size larger than it would not be washed out. As shown in the bottom-left panel of Fig.6, the long baseline is predicted for the existence of the null point, which would be an evidence of the shadow region of a black hole with high spin. The high spin causes the emission region more compact. Compared to the latest visibility detections at 1.3mm reported by Doeleman et al. (2008), only two of the five cases, with $a = 0.5$ and 0.998 , marginally reproduce the correlated density at $\sim 3.5G\lambda$ detected by the JCMT – ARO/SMT baseline. These results also suggest that the black hole is fast rotating or the inclination angle is large, which is consistent with what suggested by the previous observations at longer wavelengths. As shown in table 1, a fast rotating black hole with $a > 0.5$ predicts size of shadow less than the scattering size, so that its shadow structure is hard to resolved, especially for a highly-inclined disk. If the Galactic central black hole is really fast rotating, the future shorter wavelengths (sub-millimeter) are necessary for the detections.

We would like to thank Dr. Avery E. Broderick for useful discussion. This work is partially supported by National Basic Research Program of China (2009CB824800), the National Natural Science Foundation (10733010, 10773020, 10673010, 10573016, 10833002, 10821302), the CAS (grant KJCX2-YW-T03), and Program for New Century Excellent Talents in University.

REFERENCES

- Abramowicz, M. A., Lanza, A., & Percival, M. J. 1997, *ApJ*, 479, 179
- Bardeen, J. M., Press, W. H., & Teukolsky, S. A. 1972, *ApJ*, 178, 347
- Blandford, R. D. & Begelman, M. C. 1999, *MNRAS*, 303, L1
- Broderick, A. E., Fish, V. L., Doeleman, S. S., & Loeb, A. 2008, arXiv:0809.4490, *ApJ* in press
- Broderick, A. E. & Loeb, A. 2005, *MNRAS*, 363, 353
- . 2006a, *ApJ*, 636, L109
- . 2006b, *MNRAS*, 367, 905
- Cadez, A., Fanton, C., & Calvani, M. 1998, *New Astronomy*, 3, 647
- Carter, B. 1968, *Physical Review*, 174, 1559
- Chandrasekhar, S. 1983, *The mathematical theory of black holes* (Oxford: Clarendon Press)
- Cunningham, J. M. & Bardeen, C. T. 1973, *ApJ*, 183, 237
- Doeleman, S. & Bower, G. 2004, *Galactic Center Newsletter*, 18, 6
- Doeleman, S. S., Weintroub, J., Rogers, A. E. E., *et al.* 2008, *Nature*, 455, 78
- Ferrarese, L. & Merritt, D. 2000, *ApJ*, 539, L9
- Fish, V. L., Broderick, A. E., Doeleman, S. S., & Loeb, A. 2008, arXiv:0809.4489
- Fuerst, S. V. & Wu, K. 2004, *A&A*, 424, 733
- Gammie, C. F. & Popham, R. 1998, *ApJ*, 498, 313
- Gebhardt, K., Bender, R., Bower, G., *et al.* 2000, *ApJ*, 539, L13
- Ghez, A. M., Salim, S., Hornstein, S. D., *et al.* 2005, *ApJ*, 620, 744
- Ghez, A. M., *et al.* 2008, *ApJ*, 689, 1044
- Falcke, H., Melia, F., & Agol, E. 2000, *ApJ*, 528, L13
- Hopkins, P. F., Hernquist, L., Cox, T. J., & Kereš, D. 2008, *ApJS*, 175, 356
- Huang, L., Cai, M., Shen, Z.-Q., & Yuan, F. 2007, *MNRAS*, 379, 833
- Huang, L., Liu, S., Shen, Z.-Q., Cai, M. J. *et al.* 2008, *ApJ*, 676, L119
- Kormendy, J. & Richstone, D. 1995, *ARA&A*, 33, 581
- Manmoto, T. 2000, *ApJ*, 534, 734
- Maoz, E. 1998, *ApJ*, 494, L181
- Miller, M. C. 2006, *MNRAS*, 367, L32
- Miyoshi, M., Ishitsuka, J. K., Kamenoi, S. *et al.* 2004, *Progress of Theoretical Physics Supplement*, 155, 186
- Munyanza, F., Tsiklauri, D., & Viollier, R. D. 1998, *ApJ*, 509, L105
- Narayan, R. 2002, in *Lighthouses of the Universe: The Most Luminous Celestial Objects and Their Use for Cosmology*, ed. M. Gilfanov, R. Sunyaev, & E. Churazov (Berlin: Springer)
- Narayan, R., Mahadevan, R., Grindlay, J. E. *et al.* 1998, *ApJ*, 492, 554
- Narayan, R., Yi, I., & Mahadevan, R. 1995, *Nature*, 374, 623
- Noble, S. C., Leung, P. K., Gammie, C. F., & Book, L. G. 2007, *Classical and Quantum Gravity*, 24, 259
- Paumard, T., Perrin, G., Eckart, A., *et al.* 2005, *Astronomische Nachrichten*, 326, 568
- Peitz, J. & Appl, S. 1997, *MNRAS*, 286, 681
- Popham, R. & Gammie, C. F. 1998, *ApJ*, 504, 419
- Rauch, K. P. & Blandford, R. D. 1994, *ApJ*, 421, 46
- Rybicki, G. B. & Lightman, A. P. 1979, *Radiative processes in astrophysics* (New York, Wiley-Interscience)
- Schödel, R., Ott, T., Genzel, R., *et al.* 2003, *ApJ*, 596, 1015
- Shen, Z.-Q., Lo, K. Y., Liang, M.-C. *et al.* 2005, *Nature*, 438, 62
- Takahashi, R. 2004, *ApJ*, 611, 996
- Torres, D. F., Capozziello, S., & Lambiase, G. 2000, *Phys. Rev. D*, 62, 104012
- Tsiklauri, D. & Viollier, R. D. 1998, *ApJ*, 500, 591
- Yuan, F., Quataert, E., & Narayan, R. 2003, *ApJ*, 598, 301
- . 2004, *ApJ*, 606, 894
- Yuan, Y.-F., Narayan, R., & Rees, M. J. 2004, *ApJ*, 606, 1112
- Yuan, F., Shen, Z.-Q., & Huang, L. 2006, *ApJ*, 642, L45

APPENDIX
THE REFERENCE FRAMES

In the ADAF model, the accretion flow has both azimuthal and radial motion. Following Peitz & Appl (1997) (see also Gammie & Popham 1998, Manmoto et al 2000), we introduce three reference frames to show how to describe the velocity fields of accreted gas. The first is the locally non-rotating frame (LNRF) which is also called zero angular momentum observer (ZAMO), an orthonormal tetrad basis carried by observers whose four velocity in Boyer-Lindquist coordinates is $u^\mu = e^{-\nu}(1, 0, 0, \omega)$. The four contra-variant basis vectors of LNRF compose a matrix as follows,

$$e^\mu_{\cdot(a)}(\text{LNRF}) = \begin{bmatrix} e^{-\nu} & 0 & 0 & e^{-\nu}\omega \\ 0 & e^{-\mu_1} & 0 & 0 \\ 0 & 0 & e^{-\mu_2} & 0 \\ 0 & 0 & 0 & e^{-\psi} \end{bmatrix}, \quad (\text{A1})$$

while the four covariant basis vectors compose a matrix as follows,

$$e_{\mu}^{\cdot(a)}(\text{LNRF}) = \begin{bmatrix} e^\nu & 0 & 0 & 0 \\ 0 & e^{\mu_1} & 0 & 0 \\ 0 & 0 & e^{\mu_2} & 0 \\ -\omega e^\psi & 0 & 0 & e^\psi \end{bmatrix}. \quad (\text{A2})$$

As well known, the four rows of the matrix give four vectors in the curved space-time, whilst the four columns give four vectors in the local inertia frame, i.e. four vectors in the 'Minkovski' space-time.

The second frame is the so-call co-rotating frame, another orthonormal tetrad basis carried by observers co-rotates with the fluid with the coordinate angular velocity $\Omega = u^\phi/u^t$, i.e. whose four velocity is $u^\mu = u^t(1, 0, 0, \Omega)$. The relative physical azimuthal velocity of CRF with respect to LNRF is $V^{(\phi)} = e^{\phi-\nu}(\Omega - \omega)$, therefore, the four basis vectors of CRF can be obtained by an azimuthal Lorentz boost from these of LNRF,

$$\begin{aligned} e^\mu_{\cdot(a)}(\text{CRF}) &= \Lambda_a^{\cdot b} e^\mu_{\cdot(b)}(\text{LNRF}) \\ &= \begin{bmatrix} \gamma_\phi & 0 & 0 & \gamma_\phi\beta_\phi \\ 0 & 1 & 0 & 0 \\ 0 & 0 & 1 & 0 \\ \gamma_\phi\beta_\phi & 0 & 0 & \gamma_\phi \end{bmatrix} \begin{bmatrix} e^{-\nu} & 0 & 0 & e^{-\nu}\omega \\ 0 & e^{-\mu_1} & 0 & 0 \\ 0 & 0 & e^{-\mu_2} & 0 \\ 0 & 0 & 0 & e^{-\psi} \end{bmatrix}, \\ &= \begin{bmatrix} \gamma_\phi e^{-\nu} & 0 & 0 & \gamma_\phi(\omega e^{-\nu} + \beta_\phi e^{-\psi}) \\ 0 & e^{-\mu_1} & 0 & 0 \\ 0 & 0 & e^{-\mu_2} & 0 \\ \gamma_\phi\beta_\phi e^{-\nu} & 0 & 0 & \gamma_\phi(\beta_\phi\omega e^{-\nu} + e^{-\psi}) \end{bmatrix}. \end{aligned} \quad (\text{A3})$$

$$\begin{aligned} e_{\mu}^{\cdot(a)}(\text{CRF}) &= \Lambda^a_{\cdot b} e_{\mu}^{\cdot(b)}(\text{LNRF}) \\ &= \begin{bmatrix} \gamma_\phi(e^\nu + \beta_\phi\omega e^\psi) & 0 & 0 & -\gamma_\phi\beta_\phi e^\psi \\ 0 & e^{\mu_1} & 0 & 0 \\ 0 & 0 & e^{\mu_2} & 0 \\ -\gamma_\phi(\beta_\phi e^\nu + \omega e^\psi) & 0 & 0 & \gamma_\phi e^\psi \end{bmatrix}. \end{aligned} \quad (\text{A4})$$

The final frame is the local rest frame (LRF) of the fluid, another orthonormal tetrad basis carried by observers moving with the fluid, i.e. whose four velocity is $u^\mu = (u^t, u^r, 0, u^\phi)$. Suppose the relative physical radial velocity of LRF with respect to CRF is $V^{(r)} \equiv V$, therefore, the four basis vectors of LRF can be obtained by a radial Lorentz boost from these of CRF,

$$\begin{aligned} e^\mu_{\cdot(a)}(\text{LRF}) &= \Lambda_a^{\cdot b} e^\mu_{\cdot(b)}(\text{CRF}) \\ &= \begin{bmatrix} \gamma_r & \gamma_r\beta_r & 0 & 0 \\ \gamma_r\beta_r & \gamma_r & 0 & 0 \\ 0 & 0 & 1 & 0 \\ 0 & 0 & 0 & 1 \end{bmatrix} \begin{bmatrix} \gamma_\phi e^{-\nu} & 0 & 0 & \gamma_\phi(\omega e^{-\nu} + \beta_\phi e^{-\psi}) \\ 0 & e^{-\mu_1} & 0 & 0 \\ 0 & 0 & e^{-\mu_2} & 0 \\ \gamma_\phi\beta_\phi e^{-\nu} & 0 & 0 & \gamma_\phi(\beta_\phi\omega e^{-\nu} + e^{-\psi}) \end{bmatrix}, \\ &= \begin{bmatrix} \gamma_r\gamma_\phi e^{-\nu} & \gamma_r\beta_r e^{-\mu_1} & 0 & \gamma_r\gamma_\phi(\omega e^{-\nu} + \beta_\phi e^{-\psi}) \\ \gamma_r\gamma_\phi\beta_r e^{-\nu} & \gamma_r e^{-\mu_1} & 0 & \gamma_r\gamma_\phi\beta_r(\omega e^{-\nu} + \beta_\phi e^{-\psi}) \\ 0 & 0 & e^{-\mu_2} & 0 \\ \gamma_\phi\beta_\phi e^{-\nu} & 0 & 0 & \gamma_\phi(\beta_\phi\omega e^{-\nu} + e^{-\psi}) \end{bmatrix}. \end{aligned} \quad (\text{A5})$$

$$e_{\mu}^{\cdot(a)}(\text{LRF}) = \Lambda^a_{\cdot b} e_{\mu}^{\cdot(b)}(\text{CRF})$$

$$= \begin{bmatrix} \gamma_r \gamma_\phi (e^\nu + \beta_\phi \omega e^\psi) & -\gamma_r \beta_r e^{\mu_1} & 0 & -\gamma_r \gamma_\phi \beta_\phi e^\psi \\ -\gamma_r \gamma_\phi \beta_r (e^\nu + \beta_\phi \omega e^\psi) & \gamma_r e^{\mu_1} & 0 & \gamma_r \gamma_\phi \beta_r \beta_\phi e^\psi \\ 0 & 0 & e^{\mu_2} & 0 \\ -\gamma_\phi (\beta_\phi e^\nu + \omega e^\psi) & 0 & 0 & \gamma_\phi e^\psi \end{bmatrix}. \quad (\text{A6})$$